57th EASTERN SNOW CONFERENCE
Syracuse, New York, USA, 2000

Spatially Distributed Snow Modeling for a Comprehensive Study of the Sacramento and San Joaquin Basins, California

S.F. DALY,[1] R. DAVIS,[1] T. PANGBURN,[1] E. OCHS,[1] W. ROSENTHAL,[1]
R. AFFLECK,[1] T. BALDWIN,[1] E. BRYANT,[1] J. HARDY,[1] S. TAYLOR,[1]
H. DOTSON,[2] T. EVANS,[2] C. DUNN,[2] AND M. BURHAM[2]

ABSTRACT

This project developed, implemented, and demonstrated spatially distributed snow modeling and monitoring procedures for estimating snowmelt inputs to the Sacramento and San Joaquin river basins, California. The Distributed Snow Process Model (DSPM) used a temperature index algorithm, SSARR_grid, for estimating liquid water arriving at the ground surface each hourly time step in each model cell with 2-km spatial resolution. DSPM used interpolated air temperature and precipitation fields, as well as initial snow conditions. Air temperature interpolation incorporated hourly ambient lapse rates based on observed air temperatures in an inverse-distance-squared technique. Precipitation interpolation used an inverse-distance-squared method. We developed a linear function that specified the melt factor used by SSARR_grid in each cell depending on the accumulated temperature index. In this test, DSPM relied on maps of snow water equivalent (SWE) for initiation and validation. We estimated the spatial distribution of SWE by combining estimates of snow cover area (SCA) with interpolations of SWE based on snow sensor and course measurements. SCA retrieval algorithms used measurements from the NOAA Advanced Very High Resolution Radiometer (AVHRR) to estimate snow extent as fractional cover per pixel. SWE interpolations for this project used an algorithm similar to the temperature interpolation. The results showed that 1) SWE maps predicted by DSPM with no updating over periods up to several days have fair agreement with maps produced from AVHRR merged with ground measurements, 2) cloud cover conditions permit the construction of SWE maps from AVHRR and ground measurements with sufficient frequency to improve model results through updating, and 3) preliminary runs of HEC–HMS to route the snowmelt water capture the timing and magnitude of the flow using these spatially distributed inputs.

Key Words: snow, hydrology, modeling, remote sensing

[1] U.S. Army Engineer Research and Development Center, Remote Sensing/Geographic Information Systems Center, Hanover, New Hampshire 03755-1290, USA
[2] U.S. Army Corps of Engineers, Hydrologic Engineering Center, Davis, California, 95616, USA

INTRODUCTION

In the western United States, snowmelt contributes approximately 70–80 percent of total annual runoff. Temporal variability in snowfall at interannual scales can have dramatic impacts on land cover, agriculture, and human and nonhuman populations. Current forecasts of snow runoff volume and peak flows from montane watersheds in California and other areas throughout the western United States use spatially lumped statistical models that link indices of snow volume and melting rate to stream flow (e.g., Peck 1976). Experience shows that river flow forecasts have reasonable accuracy for any WY close to the mean of the historical record. While this family of methods for runoff forecasting makes use of data sets with several decades of observations, problems can arise when climatic conditions vary greatly from the historical mean. It appears that systematic trends in runoff timing over the last few decades may represent changes in the climate of California (Roos 1990, 1991; Pupacko 1993; Dettinger and Cayan 1995). Trends showing change also appear in the records of snow water equivalent (SWE), represented by less snow accumulation at low elevation, compared to rainfall, and more snow at high elevations (Johnson et al. 1997). These trends may have two consequences: 1) greater probability of rainfall in the winter during periods of large snow extent in areas below timberline, and 2) less snow cover in forests at the onset of spring melting. Both could lead to increases in the frequency and magnitude of peak flows (Kattelmann 1991).

Public pressure to improve runoff forecasts, water management, and apportionment continues to increase, thus motivating development of improved techniques to monitor the Sierra Nevada snow cover and track its changes. The U.S. Army Engineer Research and Development Center–Remote Sensing/GIS Center (ERDC–RS/GISC) in collaboration with the U.S. Army Corps of Engineers Hydrologic Engineering Center (HEC) continues to develop improved methods to monitor and model snow cover and runoff displayed in a common spatial context (Ochs 1997). Spatial data and spatially distributed models have not yet seen wide use or acceptance in operational forecasts of snowmelt runoff, but as competition for water resources and requirements for precision water management and control increase, the potential of using spatial data for forecast guidance and assessment of basin condition has shown increasing promise.

This paper describes the approach and first results of a continuing investigation on the use of spatially distributed modeling of snow to provide improved estimates of runoff during flood events in the Sierra Nevada, California. The tests described here implemented a spatially distributed snow model, using as simple an approach as feasible, to establish a baseline of performance against which future model developments could compare. One of the objectives of this work is to develop remote sensing as a tool for estimating snow properties to use for initiation, updating, and validation of the snow modeling approach. We chose as a case study for this paper the historic floods in California during the period December 1996 to January 1997.

METHODS

This study modeled snow properties using a simple, temperature-index approach, distributed across the watersheds of the Sacramento and San Joaquin Rivers. The test period ran from 14 December 1996 to 31 January 1997, bracketing the flood that occurred from 26 December to 4 January. The test used snow maps derived from satellite data and ground stations to specify initial snow conditions (14 December) and to compare with model predictions (23 December and 8 January). During the modeling period air temperature and precipitation were the only information input to the snow model. The snow model results included liquid water arriving at the soil surface, which was then input to a gridded runoff routing model. This paper focuses on the snow model and its inputs.

Study area

The Sacramento and San Joaquin basins drain into the great central valley of California westward from the crest of the Sierra Nevada (Fig. 1). The region ranges in elevation from about 500 m to over 4400 m in the south to just over 2700 m in the north. Of the river basins contributing to the major drainages, 75 percent have controlled flows. Approximately 15 percent of the area consists of alpine terrain with little forest cover, with an additional 25 percent of subalpine zone with continuous to discontinuous forest. The rest consists of forest, open woodland, and grasslands. In an Albers equal area projection, we specified a regular grid with 2-km resolution and considered each grid cell an independent modeling domain for snow and runoff generation. Each grid cell in the modeling approach used here has as characterization the mean elevation and forest cover.

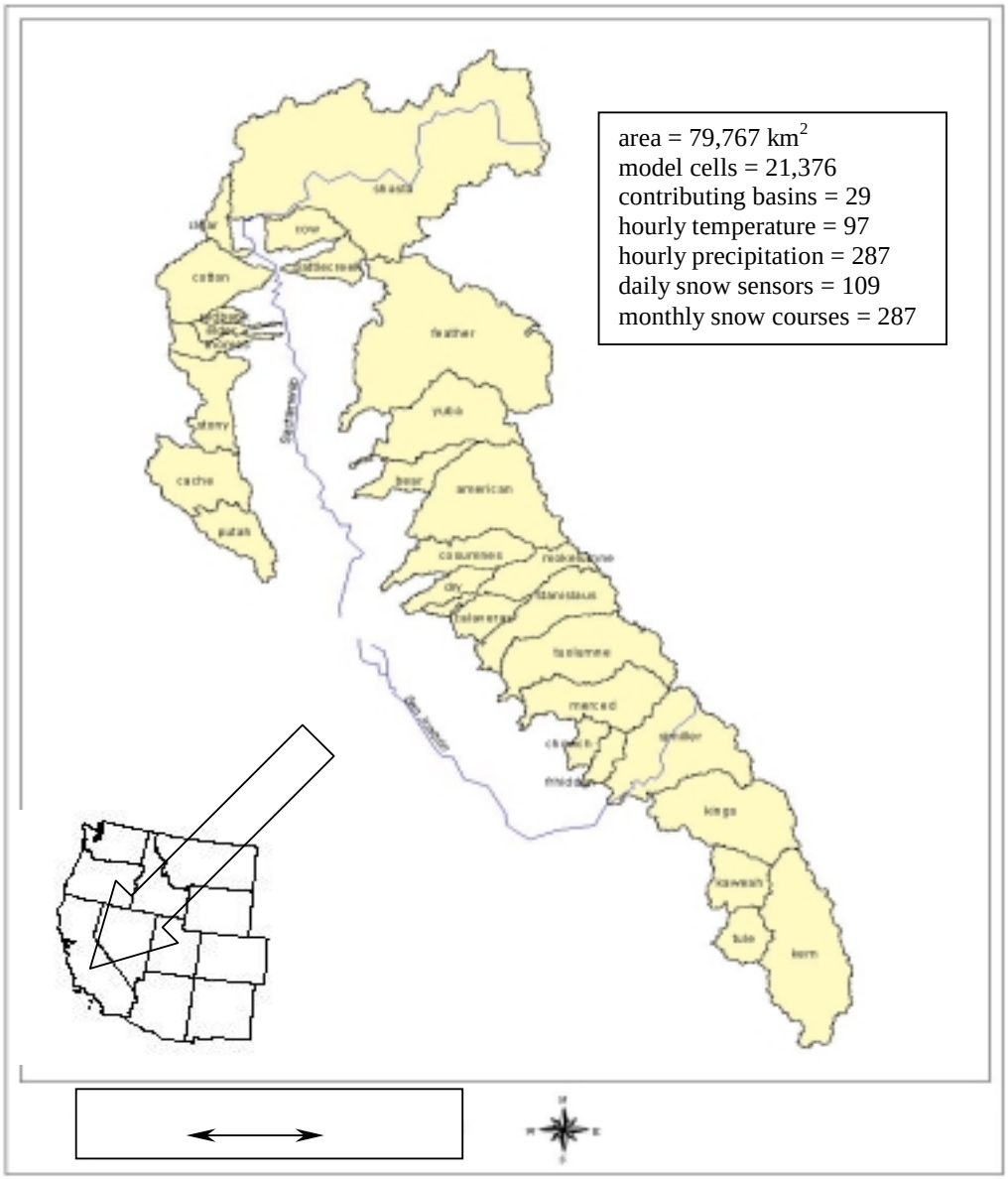

Figure 1. Sacramento and San Joaquin River basins and sub-basins, California.

Modeling the snow accumulation and ablation processes: DSPM

The Distributed Snow Process Model (DSPM) consists of a computational framework for estimating the snow conditions in the large number of distributed cells that describe a watershed or watershed sub-basin (Daly et al. 1999). The DSPM uses the standard geographic grid proposed by the Corps of Engineers Hydrologic Engineering Center (HEC), which defines cells for carrying out one-dimensional calculations of snow condition and melt production. These cells have equal area throughout the coverage using the Albers equal-area map projection. Depending on the modeling requirements, the grid resolution can vary and range from regular squares 10 m on a side to 10 km, with a 2-km grid as default used in this study. The standard hydrologic grid has the advantages of equal area property of the projection, the universal support of the Albers equal-area projection by nearly all GIS software packages, the wide use of Albers projection for a number of national mapping products, and the ease of graphical display. The DSPM cycles through all cells comprising a sub-basin during each time step, managing the data flow into and out of the snow routine as well the attributes of each cell. Currently, the DSPM uses SSARR_grid, described below, to simulate the snow processes in each grid cell. The computational framework of the DSPM allows other snow process models to be used in place of, or in conjunction with, SSARR_grid. DSPM requires of any snow model the ability to exchange information on all state variables each time step for each cell.

We developed SSARR_grid from the "Snow-Band" snowmelt computation, part of the Streamflow Synthesis and Reservoir Regulation (SSARR) model (e.g., Speers et al. 1979, Cassell and Pangburn 1991, Rockwood and Kuehl 1993). The routine estimates the liquid water available at the soil surface for a cell for one time step by applying a melt factor to a temperature index:

$$L_{free} = mf\,(T_a - T_{base})$$

where L_{free} represents the melt production and mf the melt factor, which can change in time and space. The energy available to melt snow has the index $(T_a - T_{base})$ where T_a represents the air temperature at the model cell and T_{base}, a base temperature below which the model will not allow melt.

The time step is generally controlled by the frequency of input data available and may range in time up to 24 hours; we used one hour in this study. Interpolated precipitation and air temperature drive surface processes of accumulation and melting. Currently, the temperature index method predicts snow melting with either of two options to describe the melting rate: a function of an antecedent temperature index or a predetermined function of month of the year. We used the former. Heavy rain events trigger a separate melt rate coefficient, mf_{rain}. At any point in time an antecedent temperature index describes the cold content of the snowpack, which accumulates during cold events. The model must "satisfy" the cold content before melt runoff can occur. A simple "bucket" concept provides the mechanism to retain liquid water in the snow against drainage processes until the water content reaches a user-set threshold.

Calibration of DSPM

In DSPM we chose to optimize the values in SSARR_grid of the base temperature T_{base}, the temperature used to separate rain and snow events, the rain melt factor (mf_{rain}), and the snowmelt factor mf. We developed a linear function to specify the snowmelt factor based on the accumulated temperature index. This effort used hourly temperature, SWE, and precipitation measurements during the winters 1985–1999 from 22 stations in the test region to calibrate the SSARR_grid parameters. The sum-of-squares difference between the SWE values calculated by SSARR_grid and the measured SWE was minimized using the downhill simplex method of Nelder and Mead (1965) as presented by Press et al. (1992). This method belongs to the class of multidimensional minimization procedures. The SSARR_grid used a one-hour time step during calibration.

In the first effort to calibrate the parameters of SSARR_grid we found an optimized value of each of the tuned parameters for each winter period for each station. However, we found no discernable trend between either the elevation of the station or the location of the station and the value of the optimized parameters. We decided to pool the stations and all the years of data to

produce one set of optimized results for the entire Sierra test region. This resulted in a base temperature of 32.65°F (.36°C), a temperature to separate rain and snow events of 34.97°F (1.65°C), rain melt factor of .1576, and melt factor that ranged from .0030 at an accumulated temperature index of zero to .2959 at an accumulated temperature index of 50. The melt factor was considered to be constant at higher values of the accumulated temperature index. Representative results for one location are shown in Figure 2.

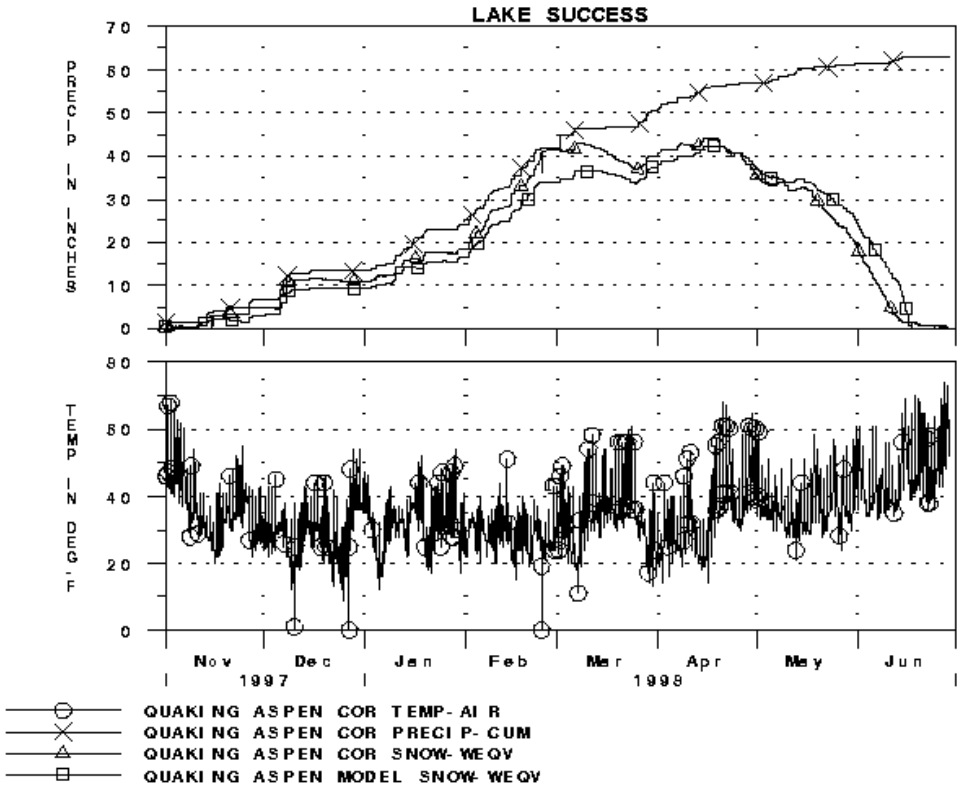

Figure 2. Calibration of the melt factor mf *using an optimization technique with measurement from the Lake Success snow sensor station. Rising trace in top plot shows cumulative precipitation, while the two similar lines below show the measured and modeled SWE. The bottom plot shows the air temperature record during this calibration period.*

Model input data: Meteorology

As summarized in Figure 1, the model test used air temperature measurements from 97 sensors that reported hourly, while precipitation included hourly measurements from 287 gages. The air temperature records have undergone quality control to flag anomalous values and fill gaps. The precipitation record experienced similar controls, except for adjustments to gage catch efficiency. Yang et al. (1998) assessed the undercatch of standard precipitation gages depending on wind speed and have shown that during windy periods unshielded gages and gages shielded with Wyoming wind screens often catch only a small fraction of the total snowfall. We ignored this effect for the model tests described here.

We used elevation trends and an inverse-distance-squared algorithm to interpolate the air temperature measurements. At each hourly time step, a linear model fit to the air temperature measurements in and around a watershed as a function of the elevation of the measurement sites estimated the mean ambient lapse rate for the previous hour. We detrended the data for elevation by lapsing the measurements down to sea level. An inverse-distance-squared algorithm filled in

the model cells between and around the measurement sites, and the data values then followed the trend line back up in elevation to reach the model input values at the elevation of each cell.

An initial assessment of the precipitation data showed no strong trends in elevation over the whole range of elevation in the study area. Greater wind speeds with elevation and openness probably accounted for much of this lack of trend. Therefore for simplicity's sake we used an inverse-distance-squared algorithm without any other trends. This approach caused the precipitation fields to have a strong "peak and pit" pattern common with this type of interpolation.

Model input data: Initial and subsequent snow conditions

For operational application we have developed methods to map SWE by merging interpolated measurements of snow water equivalent, SWE, with snow cover area, SCA, recovered from satellite measurements:

$$SWE_{\text{model cell, basin}} = SWE_{\text{interpolated}} \times SCA_{\text{satellite}}$$

where $SWE_{\text{model cell, basin}}$ represents the total volume of water equivalent on a model cell or basin, $SWE_{\text{interpolated}}$ the preliminary value from spatial interpolation of ground data, and $SCA_{\text{satellite}}$ the fractional cover of snow per pixel.

The SWE interpolation used in this study employed methods similar to those used to interpolate air temperature. The elevation trend on a daily basis provided a pattern to the interpolated field in addition to the inverse-distance-squared trends. We used measurements from both snow sensors and snow courses. On a daily basis when we did not have snow course measurements, we modeled their values using the elevation trend line. The snow measurement sites have characteristics suitable for index modeling (i.e., more and earlier snow than nearby areas), so spatial fields interpolated from these data tend to overestimate the total SWE on a watershed. While the general trends of the interpolated SWE follow ground-based surveys, multiplication with subpixel SCA improves estimation of the total SWE by introducing the spatial patterns of bare area.

We mapped fractional SCA (subpixel) using imagery from the Advanced Very High Resolution Radiometer (AVHRR), broadly following the concepts described by Rosenthal and Dozier (1996). This processing, which used three reflectance channels on the thermal band of channel 4, comprised five steps:

1. First, we interactively georegistered the imagery using a variety of reference images including vector-based hydrography, digital elevation models, and previously registered images. The registration step also binned the output into 1.0-km pixels.

2. After calibrations of the raw data and atmospheric correction of channels 1 and 2 using 6S (Vermote et al. 1997), the second step separated the reflectance component of Channel 3 (3.5–3.9 μm) from the emittance component using the temperature from channel 4 and assumptions about the surface emissivity to make a new, synthesized channel 3B.

3. As a third step, we interactively formed a cloud mask using a variety of threshold tests on individual bands and band combinations, then merged this mask with a water mask formed from the GIS hydrographic coverage. Occasionally, this step required manual image editing.

4. In the fourth step, we reduced the image space for further analyses: the algorithm first masked areas with clouds and areas too warm to contain snow using a temperature set by the user. Rosenthal (1996) describes these calculations in more detail. Next the algorithm determined which pixels could contain snow using a binary decision tree. We trained the tree on 25,532 cases built from mixtures of theoretical reflectance spectra of snow (two-stream approximation to the radiative transfer equation) and non-snow spectra derived from spectral libraries convolved to AVHRR bandwidths. For channels 1 and 2 we used the spectral data on types of granite, soil, and vegetation compiled by Satterwhite and Henley (1990), while for the extracted channel 3B we used the spectral reflectances from Salisbury and D'Aria (1994).

5. The pixels determined as likely to contain snow next ran down a regression tree to estimate the fractional cover of snow per pixel, SCA. We trained the regression tree against a set of 25,532 cases of mixtures of 23 spectra including photometric shade (0,0,0). The independent data

included channels 1, 2, and 3B and the ratios *R3-1* (channel 3/(channel 3 + channel 1) and *R3-2* (channel 3/channel 3 + channel 2) based on results from Rosenthal and Dozier (1996) with Landsat TM.

We have current tests in progress to quantitatively test the accuracy of the algorithm used in this study to recover SCA from AVHRR imagery relying on spectral unmixing of Landsat TM (Rosenthal 1996) and an extensive set of aerial photographs. Unpublished measurements from U.S. operations over Bosnia have shown accuracy of about ±6 percent. In the final step to produce the SWE maps, we multiplied SCA times the interpolated SWE, then averaged the result to cells with 2-km resolution.

Snow runoff modeling and routing

The Hydrologic Engineering Center's Hydrologic Modeling System (HEC–HMS), the Corps' "next-generation" software for precipitation runoff simulation, provides a variety of options for simulating precipitation runoff processes and includes its own graphical user interface, integrated hydrologic analysis components, data storage and management capabilities, and graphics and reporting facilities. We used the ModClark method, a linear distributed-runoff transformation that accepts gridded snowmelt or rainfall data (Peters and Easton 1996). DSPM estimated the snowmelt arriving at the soil surface in each cell, as described above. After calibration (Hydrologic Engineering Center 1990), HEC–HMS tracked liquid water uniquely for each cell of the study area for each time step. The ModClark method lagged and routed snowmelt runoff from each cell to the basin outlet through a series of linear reservoirs. The method summed the outflows from each linear reservoir and added baseflow to obtain the total snowmelt hydrograph in each basin. We used general trends of the discrepancies between observed and modeled hydrographs to make qualitative assessments of snow model performance.

RESULTS

Floods of 29 December 1996–4 January 1997

A series of rainstorms 29 December 1996 through 4 January 1997 brought unusually warm and heavy precipitation to the northern region of the study area. Individual storm periods ranged from 10- to 200-mm mean maximum 24-hour precipitation, while the mean of maximum accumulation across the sites for the other storm types outside the flooding period ranged from about 10 to 80 mm. The rain caused widespread snowmelt from a preexisting above-normal snowpack. These conditions caused widespread minor-to-record-breaking floods from central California to Oregon, during which several gaging stations recorded the highest peaks in the history of their operation. Figure 3 shows the cumulative precipitation during the model test period. Despite obvious effects caused by the interpolation technique, the regional pattern of heavy precipitation over the northern Sierra dominates the overall pattern.

Snow extent during test period

Associated with the buildup of above-average snowpack prior to the onset of the series of rain storms came an increase in the area of the snowpack. After the floods, the satellite imagery showed a large drop in SCA, in turn associated with large volumes of snow melted by the meteorological events during the storms. Figure 4 shows composite scenes from AVHRR acquired on 14 December and 23 December 1996 and 8 January 1997. SCA from the 14 December scene defined the extent of model cells containing snow and its product with interpolated SWE the initial water equivalent in each cell.

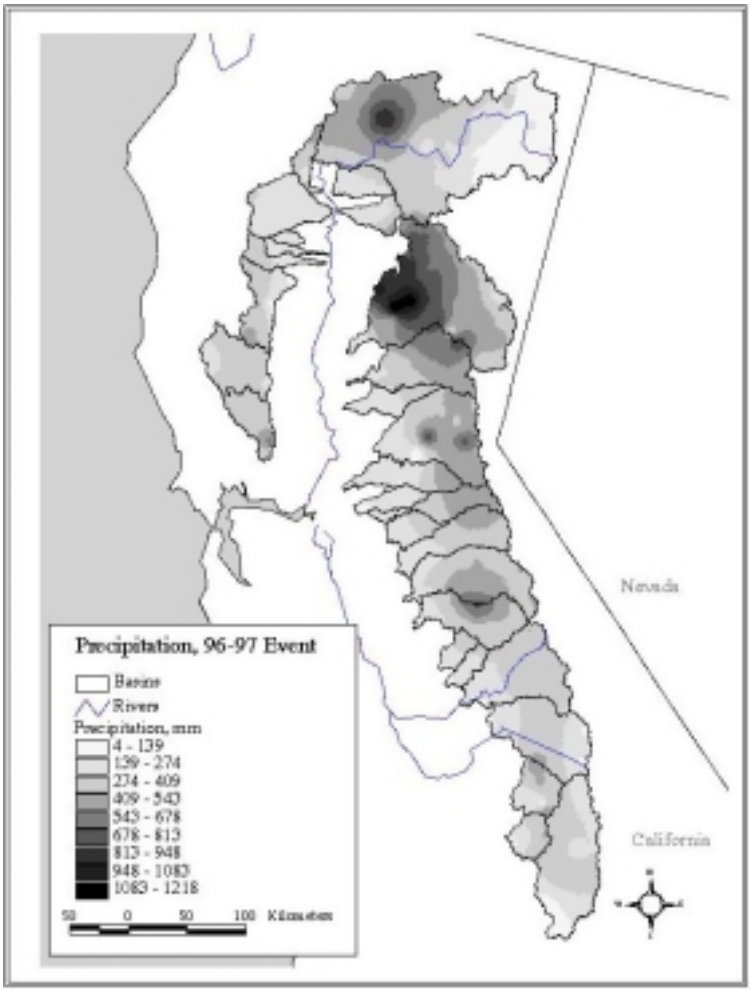

Figure 3. Total accumulated precipitation 14 December 1996 to 31 January 1997 showing patterns from use of inverse-distance-squared interpolation technique.

Model and estimated SWE during the test period

The SWE predicted by DSPM shows systematic under-prediction with increasing time when compared to the measurements by the snow sensors in the contributing basins. We compared the modeled SWE in the 2- × 2-km cell with the closest centroid to each snow sensor on a daily basis. The mean of the differences and standard deviations across larger areas of the test region showed this trend. Figures 5–7 show the time series of mean error accumulation and the standard deviation for the Tulare River basin in the southern Sierra, the San Joaquin River basin in the central Sierra, and the Sacramento River basin in the northern Sierra. In these plots one can see a rise in error rate during storms, followed by a decrease. But the decrease does not take the mean error back to zero in most cases. The reduction in error following 2–3 days after storms happens when the new SWE has fully registered on the sensor. Because of gradual snow settlement, it typically takes hours to days before new snow presents a signal to the sensors. This increases with greater antecedent snow.

Water control decision makers would have the most interest in the flooding period 26 December to 4 January. Thus the snow conditions just before the event and just after the event provide suitable evidence for assessing how this approach performed in an extreme event. We compared the SWE predicted by DSPM with the SWE maps derived from AVHRR and interpolated ground measurements on 23 December and 8 January, two dates for which we had relatively complete

SCA maps. Figures 8 and 9 show the differences on a cell-by-cell basis between the SWE predicted by DSPM and the satellite-derived SWE product. The least differences occurred in the lower elevation where the snowpack has not reached great depths of SWE (SWE < 200 mm), but had reached great extent (see Fig. 3). The greatest differences, both positive and negative, on both dates occurred in the alpine and subalpine areas, particularly in the southern Sierra. In the context of this case study this distribution of error proved fortuitous, as we show in the next section. The areas with most error contributed the least runoff, in general, to the maximum observed streamflow. Figure 10 shows the runoff/precipitation ratio for the event, which backs up this statement.

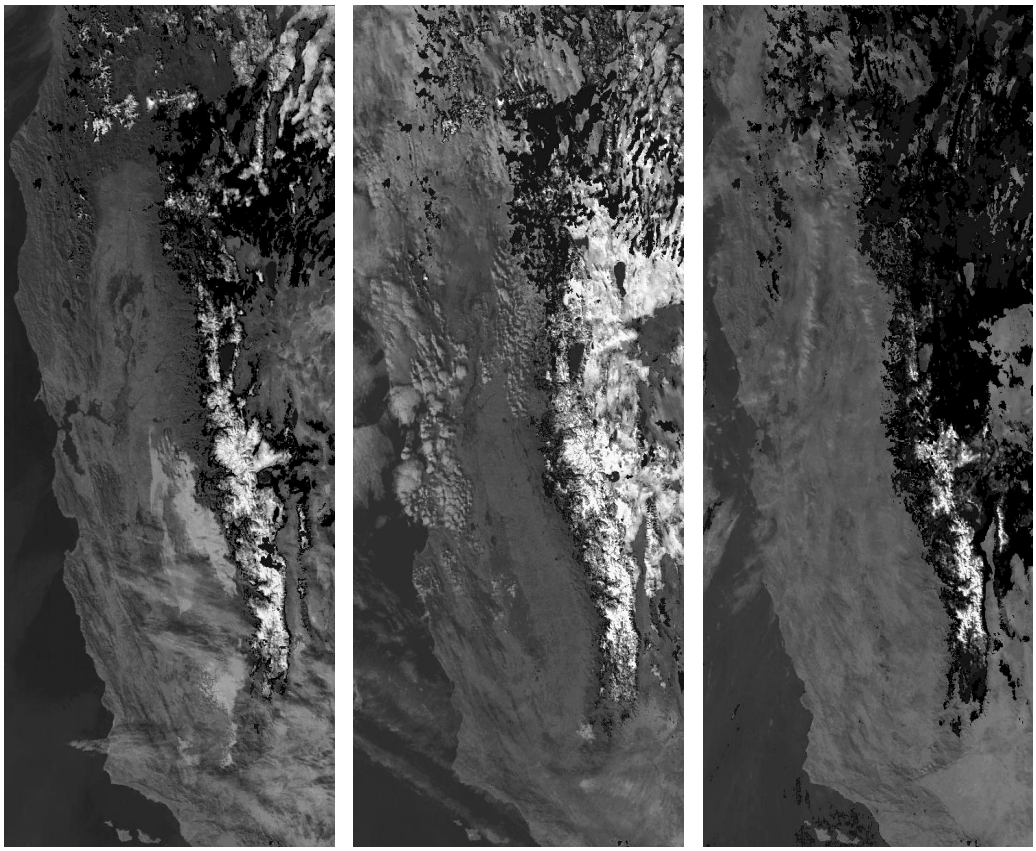

Figure 4. Composite scenes from AVHRR acquired on 14 December and 23 December 1996 and 8 January 1997. Light gray background formed as gray shade image composite of AVHRR channels 3, 2, and 1. The maximum snow extent during the test period shows as the black masked area. Inside this area SCA shows as white (SCA = 100%) to dark gray (SCA has low fraction). Homogeneous dark gray areas represent cloud over the maximum area of snow cover (the mask).

Model and observed runoff: Selected examples

Detailed analysis of the performance of the snow model in relation to the observed and predicted hydrographs lies beyond the scope of this paper, but will appear in future articles. We present instead typical results from a basin hardest hit by flooding, the American River basin (see Fig. 1), and typical results from high-elevation basins in the alpine and subalpine zones of the Sierra. Figure 11 shows the output graphics from HEC–HMS for a stream gage on the American River, which demonstrates that the modeling system can achieve correct prediction of the timing of the peak flow and reasonable prediction of the magnitude of the peak flow. Figure 12 shows similar output graphics from a high elevation watershed that demonstrates the problems with combined error from incorrect precipitation and probable problems with how the model stored

meltwater. Both the predicted total volume and flow timing show large discrepancies with the observed flow.

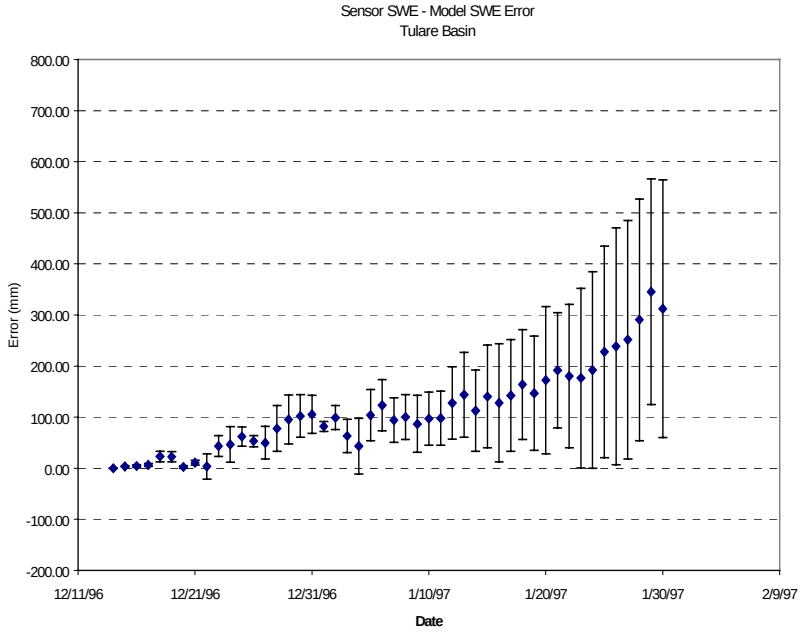

Figure 5. Plot of accumulating error with time of the SWE predicted by DSPM at sensor sites and the measurements reported by those sites. The mean of the differences between the model and measurements across the Tulare basin (southern Sierra) shows as the symbols in the center of the error bars. Error bars show the standard deviation of the mean differences.

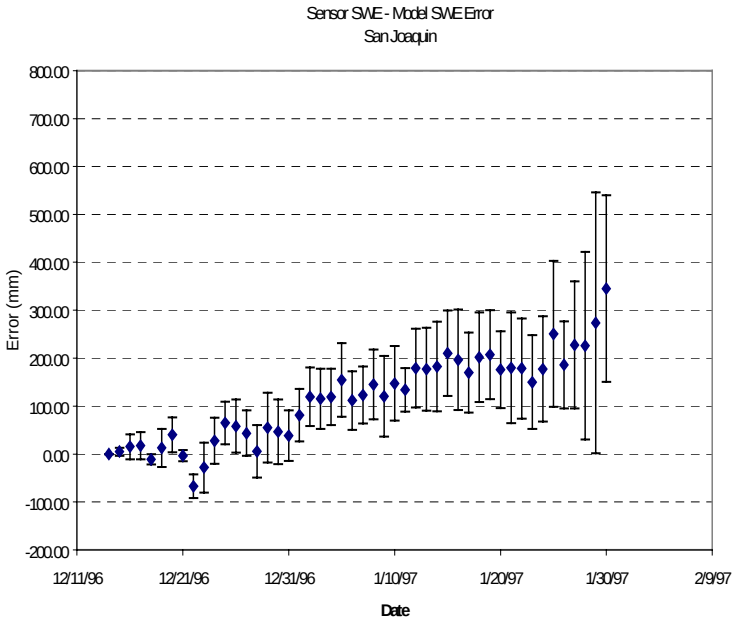

Figure 6. Plot of accumulating error with time of the SWE predicted by DSPM at sensor sites and the measurements reported by those sites. The mean of the differences between the model and measurements across the San Joaquin basin (central Sierra) shows as the symbols in the center of the error bars. Error bars show the standard deviation of the mean differences.

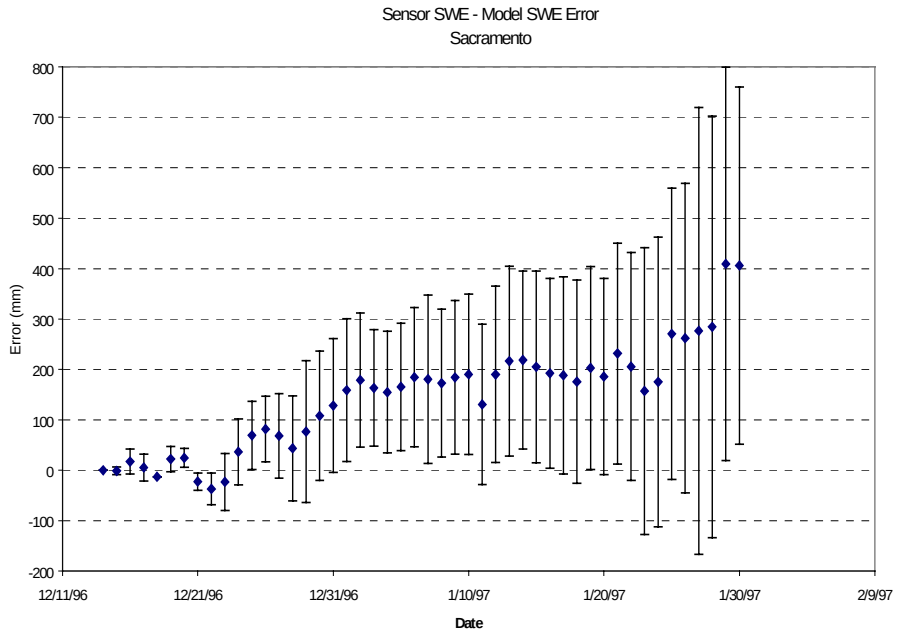

Figure 7. Plot of accumulating error with time of the SWE predicted by DSPM at sensor sites and the measurements reported by those sites. The mean of the differences between the model and measurements across the Sacramento basin (northern Sierra) shows as the symbols in the center of the error bars. Error bars show the standard deviation of the mean differences.

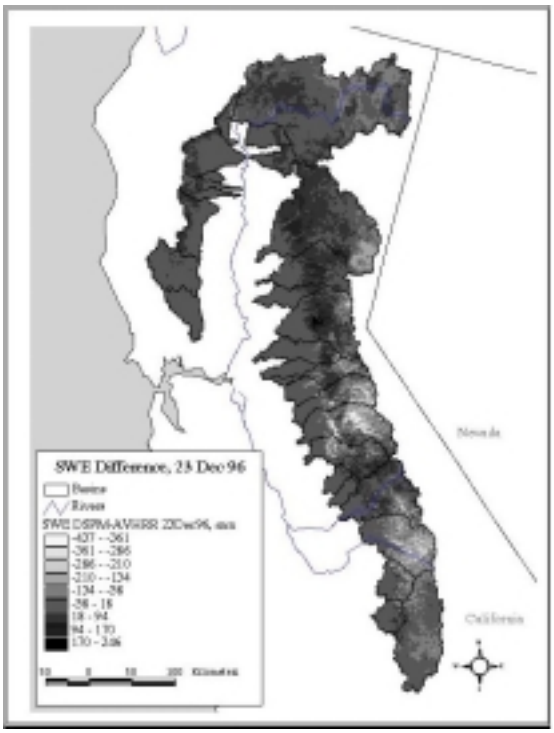

Figure 8. The difference between the SWE predicted by DSPM and the SWE estimated by merging AVHRR-derived SCA with interpolated ground measurements shown for 23 December 1996.

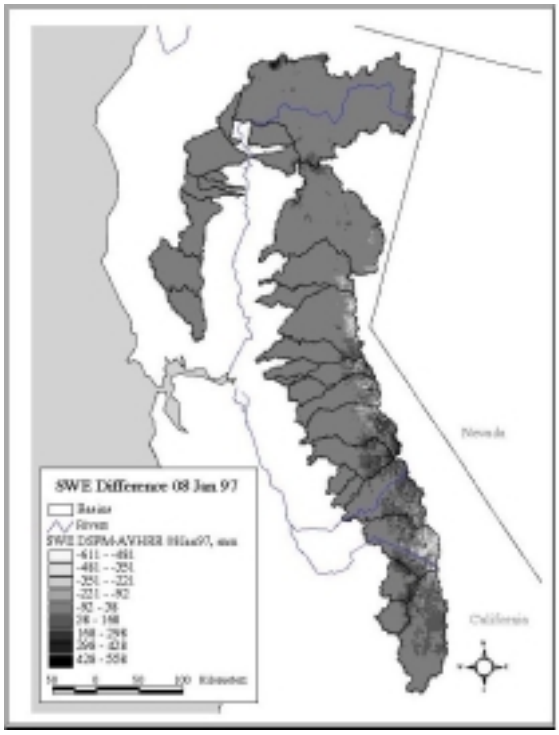

Figure 9. The difference between the SWE predicted by DSPM and the SWE estimated by merging AVHRR-derived SCA with interpolated ground measurements shown for 8 January 1997.

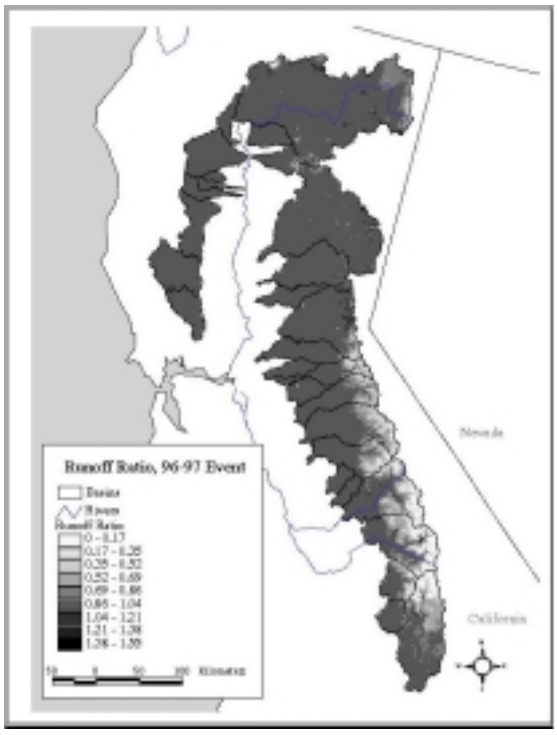

Figure 10. The ratio of precipitation input to runoff produced by the 1996–1997 flooding event. Compare area with low runoff production with 8 January AVHRR SCA map shown in Figure 4.

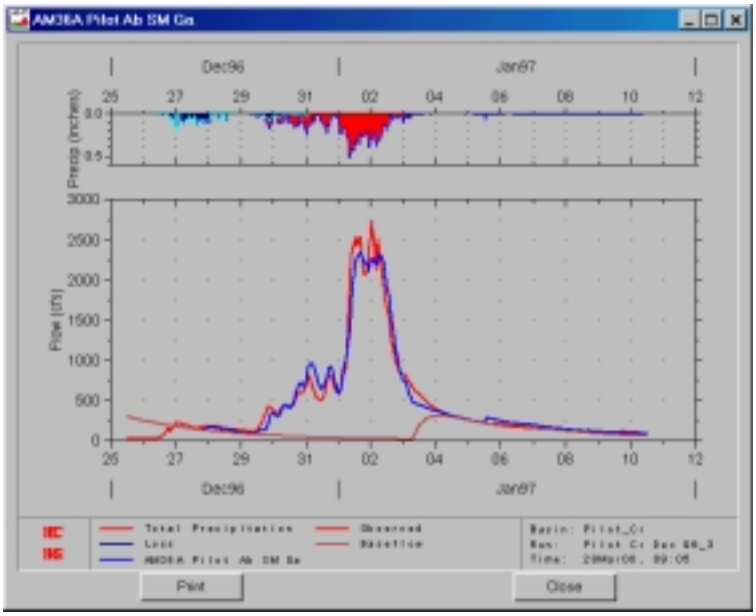

Figure 11. Graphical output from HEC-HMS, a model that routes spatially distributed inputs to runoff. The upper graph shows snowmelt, precipitation, and combined inputs to this heavily flooded tributary of the American River. The lower plot shows the predicted and observed flows. The predictions overestimate the early peaks, while underestimating the main flow peak.

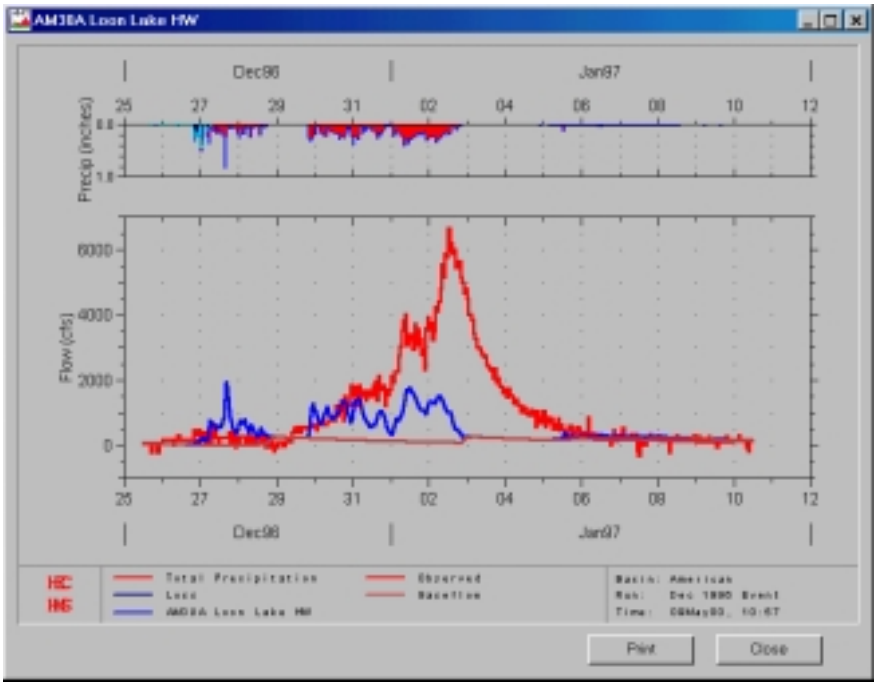

Figure 12. Graphical output from HEC-HMS, a model that routes spatially distributed inputs to runoff. The upper graph shows snowmelt, precipitation, and combined inputs to this heavily flooded tributary of the American River. The lower plot shows the predicted and observed flows. The predictions show an earlier peak than observed and the predicted flow represents much less volume than observed.

SUMMARY AND CONCLUSIONS

This paper reports on a study that implemented a simple approach to modeling processes of snow hydrology with explicit spatial distribution. The model employed snow cover products derived from remote sensing, operational ground-based measurements of snow, air temperature and precipitation, and observed streamflow. The snow model DSPM used parameters that resulted from optimized calibration over many sites and for many storms. Air temperature measurements drove the snow model calculations after interpolation that expressed the elevation trends. A simple approach interpolated precipitation, which showed weaknesses in the results. The model predicts less SWE than observed and this systematic error increases over time. However, assimilation of the satellite SWE product could improve model performance even without changing the procedures. We conclude the following:

- This spatially distributed approach to use a simple snow model over a large region captures the general trends in observed snow water equivalent and runoff over time periods up to several days.
- In the context of this case study, the New Year's floods of 1997, this modeling approach captured the snow depletion and runoff dynamics over the area that contributed most to maximum flows. These areas had relatively shallow snow and little ambiguity in precipitation type, rain or snow.
- Much work remains to develop more appropriate techniques to adjust measurements of precipitation gages in the absence of wind speed measurements in the alpine and subalpine zones.
- The SWE maps built from merging AVHRR-derived SCA and interpolated SWE provide suitable data for initiating and validating this type of modeling approach. We conclude by proxy that this product would improve the model performance through its use to update model state variables.
- Comparison of modeled SWE with sensor-measured SWE shows that DSPM underpredicted SWE systematically, thus reflecting problems in our interpolation of precipitation and probably how the model handles water storage in deep packs.

ACKNOWLEDGMENTS

The U.S. Army Engineer Sacramento District, Water Management Section (CESPK-ED-D), provided the primary resources supporting preparation of this paper. The Corps Civil Works Remote Sensing Research Program, Work Unit CWIS 32039, supported development of the snow mapping science and technology, along with NASA EOS IDS Grant NAG5-4814. Funds to develop and implement DSPM came from the Corps Northwest and Mississippi Valley Divisions. We also gratefully acknowledge support from the NASA project Earth System Science Workbench of the University of California Santa Barbara, part of the Earth Science Information Partners (ESIP) Federation, which provides guidance on AVHRR imagery and additional support to improve subpixel mapping of snow extent. The NASA Southwest Earth Science Applications Center at the University of Arizona supports continued research to develop methods to map snow water equivalent in montane environments and the development of methods to use mesoscale climate analyses to drive the models.

REFERENCES

Cassell, E.A., and T. Pangburn (1991) Interactive modeling of cold regions watersheds with SSARR. In *NHRI Symposium on Northern Hydrology: Selected Perspectives* (T.D. Prowse and

C.S.L. Ommanney, Ed.). Environment Canada, National Hydrology Research Institute, No. 6, 363–377.

Daly, S.F., E. Ochs, E. Davis, and T. Pangburn (1999) Distributed Snow Process Model for use with HEC–HMS. In *Proceedings, ASCE Conference on Cold Regions Engineering*, American Society of Civil Engineers, 538–549.

Dettinger, M.D., and D.R. Cayan (1995) Large-scale atmospheric forcing of recent trends toward early snowmelt runoff in California. *Journal of Climate*, 8: 606–623.

Hydrologic Engineering Center (1990) HEC-1 Flood Hydrograph Package, User's Manual, U.S. Army Corps of Engineers, Davis, California.

Johnson, T., J. Dozier, J. Michaelsen, P. Fohl (1997) River basin variations in Sierra Nevada accumulation trends. In *Proceedings, Joint 54th Eastern Snow Conference and 65th Western Snow Conference*, 310–316.

Kattelmann, R.C. (1991) Peak flows from snowmelt runoff in the Sierra Nevada USA. In *Snow, Hydrology and Forests in High Alpine Areas* (H. Bergman et al., Ed.). IAHS Publication No. 205: 203–211.

Nelder, J.A., and R. Mead (1965) A Simplex method for function minimization. *Computer Journal*, 7: 308–313.

Ochs, E. (1997) CorpsView: A Water Control System Visualization Tool. Description Document, U.S. Army Corps of Engineers, Engineer Research and Development Center, Cold Regions Research and Engineering Laboratory, Remote Sensing/GIS Center, Hanover, New Hampshire, 9 p.

Peck, E.L. (1976) Catchment modeling and initial parameter estimation for the National Weather Service river forecast system. Technical Memorandum, U.S. National Oceanic and Atmospheric Administration, NWS HYDRO-31, June 1976, 24 p.

Peters, J., and D. Easton (1996) Runoff simulation using radar data. *Water Resources Bulletin*, American Water Resources Association, 32(4): 753–760.

Press, W.H., et al. (1992) Numerical Recipes. New York: Cambridge University Press.

Pupacko, A. (1993) Variations in northern Sierra Nevada streamflow: Implications of climate change. *Water Resources Bulletin*, American Water Resources Association, 29(2): 283–290.

Rockwood, D.M., and D.W. Kuehl (1993) Interactive calibration for the SSARR watershed model. *Proceedings, Joint 50th Eastern Snow Conference and 61st Western Snow Conference*, 273–281.

Roos, M. (1990) Possible climate change and its impact on snowmelt water supply in California. In *Proceedings, 58th Western Snow Conference*, 130–136.

Roos, M. (1991) Trend of decreasing snowmelt runoff in northern California. In *Proceedings, 59th Western Snow Conference*, 29–36.

Rosenthal, W. (1996) Automated snow mapping at subpixel resolution from NOAA–AVHRR data. Final report: Programs for estimating subpixel snow-covered area. Technical Report, U.S. Army Cold Regions Research and Engineering Laboratory, Hanover, New Hampshire, 35 p.

Rosenthal, W., and J. Dozier (1996) Automated mapping of montane snow cover at subpixel resolution from the Landsat Thematic Mapper. *Water Resources Research*, 32(1): 115–130.

Salisbury J.W., and D.M. D'Aria (1994) Emissivity of terrestrial materials in the 3–5 μm atmospheric window. *Remote Sensing of Environment*, 47: 345–361.

Satterwhite, M.B., and J.P. Henley (1990) Hyperspectral signatures (400 to 2500 nm) of vegetation, minerals, soils, rocks, and cultural features: Laboratory and field measurements. U.S. Army Corps of Engineers, Engineering Topographic Laboratories, Fort Belvoir, Virginia, ETL-0573.

Speers, D., D. Kuehl, V. Schermerhorn (1979) Development of the operational snow band SSARR model. In *Proceedings, Meeting on Modeling of Snow Cover Runoff, 26–28 September 1978, Hanover, New Hampshire* (S.C. Colbeck and M. Ray, Ed.). USA Cold Regions Research and Engineering Laboratory Special Report SR 79-36, 369–378.

Vermote, E.F., D. Tanré, J.L. Deuzé, M. Herman, and J.-J. Morcrette (1997) Second simulation of the satellite signal in the solar spectrum, 6S: An overview. *IEEE Trans. Geoscience and Remote Sensing*, 35(3): 675–686.

Yang, D.Q., B.E. Goodison, J.R. Metcalfe, V.S. Golubev, R. Bates, T. Pangburn, and C.L. Hanson (1998) Accuracy of NWS 8" standard nonrecording precipitation gauge: Results and application of WMO intercomparison. *Journal of Atmospheric and Oceanic Technology*, 15(1) pt. 1: 54–68.